

Article

# High-Resolution Observations of Upwelling and Front in Daya Bay, South China Sea

Huabin Mao <sup>1,2,3</sup>, Yongfeng Qi <sup>1,4,\*</sup>, Chunhua Qiu <sup>5</sup>, Zhenhua Luan <sup>6</sup>, Xia Wang <sup>1,4</sup>, Xianrong Cen <sup>4</sup>, Linghui Yu <sup>1,4</sup>, Shumin Lian <sup>1</sup> and Xiaodong Shang <sup>1,3,4</sup>

<sup>1</sup> Key Laboratory of Science and Technology on Operational Oceanography, South China Sea Institute of Oceanology, Chinese Academy of Sciences, Guangzhou 510301, China; maohuabin@scsio.ac.cn (H.M.); wangxia@scsio.ac.cn (X.W.); lhyu@scsio.ac.cn (L.Y.); smlian@scsio.ac.cn (S.L.); xdshang@scsio.ac.cn (X.S.)

<sup>2</sup> Ocean College, Zhejiang University, Zhoushan 316021, China

<sup>3</sup> Southern Marine Science and Engineering Guangdong Laboratory (Guangzhou), Guangzhou 511458, China

<sup>4</sup> State Key Laboratory of Tropical Oceanography, South China Sea Institute of Oceanology, Chinese Academy of Sciences, Guangzhou 510301, China; xrcen@scsio.ac.cn

<sup>5</sup> School of Marine Sciences, Sun Yat-sen University, Guangzhou 510275, China; qiuchh3@mail.sysu.edu.cn

<sup>6</sup> State Key Laboratory of Nuclear Power Safety Monitoring Technology and Equipment, China Nuclear Power Engineering Co., Ltd., Shenzhen 518124, China; zhenhualuan@cgnpc.com.cn

\* Correspondence: yfqj@scsio.ac.cn



**Citation:** Mao, H.; Qi, Y.; Qiu, C.; Luan, Z.; Wang, X.; Cen, X.; Yu, L.; Lian, S.; Shang, X. High-Resolution Observations of Upwelling and Front in Daya Bay, South China Sea. *J. Mar. Sci. Eng.* **2021**, *9*, 657. <https://doi.org/10.3390/jmse9060657>

Academic Editor:  
Charitha Pattiaratchi

Received: 13 May 2021

Accepted: 11 June 2021

Published: 13 June 2021

**Publisher's Note:** MDPI stays neutral with regard to jurisdictional claims in published maps and institutional affiliations.



**Copyright:** © 2021 by the authors. Licensee MDPI, Basel, Switzerland. This article is an open access article distributed under the terms and conditions of the Creative Commons Attribution (CC BY) license (<https://creativecommons.org/licenses/by/4.0/>).

## 1. Introduction

The South China Sea (SCS) is the largest marginal sea connected to the Western Pacific and is dominated by the East Asian monsoon. In winter, northeasterly winds overlie the SCS, whereas in summer, southwesterly winds prevail across the region [1,2]. In the Northern SCS, surface currents (e.g., the Kuroshio Current, South China Sea Warm Current, and cyclonic currents) display complicated dynamics. All of these large-scale currents are generally associated with wind, wind stress curl, and the processes from the Pacific [3–7].

Mesoscale to small-scale structures prevail in shelf seas of the Northern SCS, including eddies, fronts, and upwellings/downwellings [8]. These features play very important roles in regulating oceanic heat and energy exchange, are vital to the transport of biochemicals, and influence interannual/decadal climate variations [9]. Daya Bay (DYB) is located in the subtropical ocean and is one of the largest and most important gulfs along the southern coast of China. Physical and biochemical processes in DYB have been the focus of many previous studies. Thermal pollution has been identified in the vicinity of a nuclear power

station in DYB [10]. High dissolved oxygen (DO) and nutrient concentrations were reported to be trapped within surface water [11,12]. The investigators surmised that the high surface nutrient concentrations resulted from stratification and the intrusion of upwelling water. The water refresh time was found to be approximately 26 days and wind driven. Fronts and associated eddies have been widely reported by oceanographers in Southern California [13], Africa [14], and Alaska [15]. Coastal fronts have mainly been examined at the interface of coastal water and the open ocean. According to their different formation mechanisms, coastal fronts can include tidal mixed, river plume, continental-shelf, upwelling, cape, and island fronts. Both eddies and fronts have mainly been observed via satellite or in situ ship-based observations.

Understanding the small-scale physical and biological processes in coastal and estuarine areas is a pressing issue in oceanography. In recent studies, small-scale physical processes in these areas have been observed [11,16,17]. Anthropogenic activities are considered the most important factor in the degradation of the DYB marine environment in recent years [10,18]. Therefore, studies of the hydrological and ecological processes in DYB are important for understanding the impacts of human activities on the ecology of DYB. Fixed-site and remotely sensed observations are commonly used in these studies [10,19–22]. For example, Tang et al. [10] obtained remote-sensing data from the Advanced Very High-Resolution Radiometer (AVHRR) satellite to study the thermal plume discharged by the nuclear power station into DYB and analyze its seasonal characteristics. Sun et al. [19] and Yang et al. [22] studied the long-term changes in phytoplankton response patterns in DYB, using fixed-site observations. However, satellite remote-sensing and fixed-site station observations have a disadvantage in that these observational methods cannot be used to obtain high-resolution internal profile characteristics. Satellite remote-sensing observation can only observe sea surface information. In situ conductivity–temperature–depth profiler (CTD) observation of fixed-site station often lacks continuity of spatial and temporal results.

Daya Bay covers an area of 600 km<sup>2</sup>, with a width of approximately 15 km and a north to south length of approximately 30 km. It has a complex topography, contains many islands, and therefore, has a rich dynamic structure. Low-resolution station observations cannot be used to explain the structure of the fine-scale, dynamic thermal, and ecological processes in the bay. A useful method for observing oceanic processes is towed observation. With this method, high-resolution data can be obtained rapidly and continuously. In this study, we investigated the rich structural characteristics of DYB, which included the thermal plume discharged from the nuclear power station, as well as an upwelling, and front, using high-resolution Yoing Ocean Data Acquisition (YODA) profiler data and a microstructure turbulence profiler. We then describe the fine-scale and turbulence features of these structures.

## 2. Materials and Methods

### 2.1. Instruments

The main data used in the study were collected by a YODA profiler and a VMP-250 turbulence profiler.

The YODA profiler (manufactured by JFE Advantech Co. Ltd., Japan; Figure 1a) is a tow-yo instrument that can be used to profile the water column with high resolution from small boats, without occupying much space [11]. The instrument is equipped with a deployment winch and sensors that measure conductivity, temperature, pressure, chlorophyll, turbidity, and DO. The brush at the top of the instrument provides a stabilizing effect on the free-fall sinking speed, which is approximately constant at 0.2 m/s. The sampling frequency is 10 Hz. All data are stored internally and downloaded to a PC through a wet connector and interface.



**Figure 1.** (a) The Yoing Ocean Data Acquisition (YODA) profiler. (b) The VMP-250 turbulence profiler.

The VMP-250 (manufactured by Rockland Scientific inc., Canada; Figure 1b) is a coastal-zone profiler for the measurement of microscale turbulence. The profiler is designed for operation off small vessels with limited deck space (e.g., zodiacs) or where electrical power facilities are limited or missing (e.g., ice camps). The instrument is equipped with two shear probes, one thermistor, and a nose-mounted conductivity–temperature sensor. The VMP-250 has a constant free-fall sinking speed of approximately 0.7 m/s. The sampling frequency is 1024 Hz. All data are stored internally and downloaded to a PC through a wet connector and interface.

## 2.2. Observations

DYB is a large semi-enclosed bay (ca. 24 km in length and 13–25 km in width, covering an area of ca. 600 km<sup>2</sup>). The bay has an irregular coastline and contains more than 50 islands. It is located along the south coast of China (114°29.7'–114°49.7' E, 22°31.2'–22°50.0' N), as shown in Figure 2. Measurements were taken between 20 October and 22 October 2015. On 20 October 2015, we obtained conductivity, temperature, pressure, chlorophyll, turbidity, and DO data, using YODA along the western boundary of DYB (S1) and a cross-section of the mouth of the bay (S2) (Figure 2). The S1 observation transect ran from the north to the south, with the survey starting at 12:20 local time and ending at 14:50, whereas S2 ran from the west to the east, with the survey starting at 16:00 and ending at 18:30. During the cruise, YODA obtained 53 and 56 profiles at S1 and S2, respectively. The average space interval between successive YODA measurements was approximately 230 m, enabling fine-scale observations of physical phenomena.

The VMP-250 profiler was used to measure turbulence at a fixed station at the mouth of DYB (yellow triangle in Figure 2b). We obtained 74 turbulence profiles from 10:00 on 21 October to 7:30 on 22 October 2015. The time intervals between VMP-250 measurements ranged from 10 to 30 min; therefore, any rapid changes in physical phenomena could be observed.

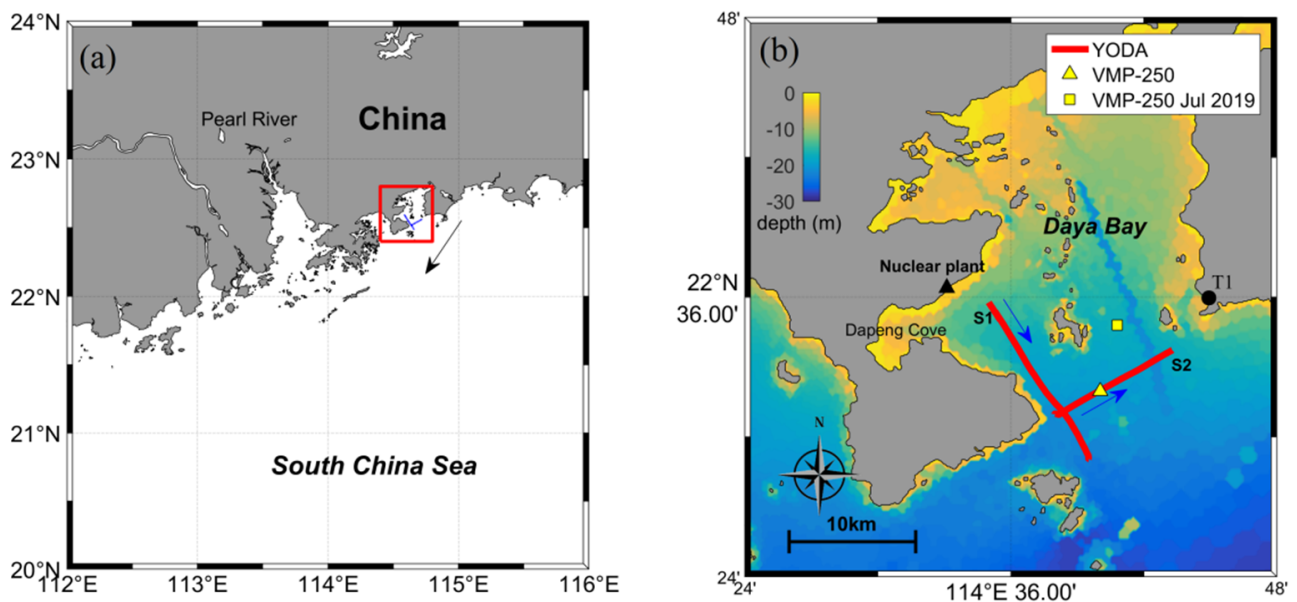


**Figure 2.** (a) Location of Daya Bay (DYB) along the southern coast of China. The arrow indicates the sea wind direction. (b) Bathymetric map of DYB, in which S1 and S2 indicate the two YODA observation transects (red lines). The yellow triangle and square indicate the locations of VMP-250 profiler observations and the blue arrows indicate vessel route directions. T1 (black circle) is the observation station of tidal elevation.

There are no major rivers discharged into DYB, but three small streams discharged into Dapeng Cove. From September to October 2015, the average rainfall in DYB is less than 30 mm. The sea surface wind was northeasterly and was less than 10 m/s during the observation period, indicating that our observation was less affected by surface runoff and sea surface wind field. Therefore, the effects of rainfall, runoff and sea surface wind are ignored in the latter analysis. The tidal current in DYB is characterized by diurnal tide and semidiurnal tide and the semidiurnal tide is more prominent ([18]).

### 2.3. Calculation of Turbulence

The shear probes in the VMP-250 profiler measured high-frequency velocity fluctuations, which were used to calculate the local turbulent dissipation rate. The dissipation rate was estimated by using the following isotropic formula:

$$\varepsilon = \frac{15}{2} \bar{v} \left( \overline{\frac{\partial u}{\partial z}} \right) = \frac{15}{2} \bar{v} \int_0^{k_{max}} \psi(k) dk \quad (1)$$

where  $\nu$  is the kinematic molecular viscosity, the overline indicates a spatial average,  $u$  is either one of the two horizontal components of velocity,  $z$  is the vertical coordinate,  $\psi(k)$  is the spectrum of vertical shear, and  $k$  is the vertical wavenumber [23]. The upper limit of the integration,  $k_{max}$ , is variable. The  $k_{max}$  value was calculated by using the method recommended by Shang et al. [24], which states that it should be the smallest of the following values: the lowest frequency that shows corruption of the shear signal by vibrations, a wavenumber of 150 cpm due to the spatial resolution of the shear probe, the cutoff frequency of the antialiasing filter, an estimate of the wavenumber that resolves 90% of the shear variance according to the Nasmyth spectrum, using the method of Lueck [25], or the location of the spectral minimum determined with a low-order fit to the spectrum in log-log space. Diapycnal diffusivity [23] was calculated based on the dissipation rate ( $\varepsilon$ ) and stratification as follows:

$$\kappa_\rho = \Gamma \frac{\varepsilon}{N^2} \quad (2)$$

where  $\Gamma$  is the mixing efficiency, which was set to 0.2. The stratification was calculated as follows:  $N^2 = -\frac{g}{\rho} \frac{\partial \rho}{\partial z}$ , where  $g$  is the acceleration due to gravity.

#### 2.4. A Workflow Graph

Figure 3 provides a workflow graph to recap on the logic path of the study. The workflow mainly consists of three parts, including the used instruments, the data types, and the observed costal phenomena.

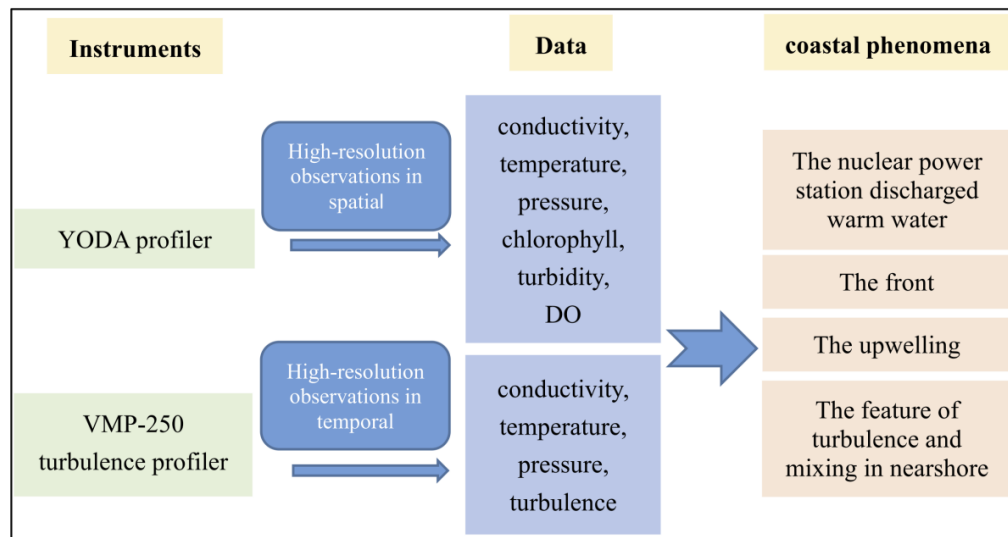


**Figure 3.** The workflow graph to recap on the logic path of the study.

### 3. Results

#### 3.1. High-Resolution Observations by YODA

In the section, features of coastal phenomenon, including the nuclear power station discharged warm water, upwelling and front, are revealed by high spatial resolution observations by YODA.

##### 3.1.1. Water Properties

Our efforts to obtain high-resolution data for DYB by using the YODA profiler proved to be successful. Figures 4 and 5 show the observed data, which indicated that the water environment of DYB was complex, with obvious horizontal spatial and vertical differences in temperature and salinity characteristics. The temperature varied from 26.2 to 27.4 °C, and salinity varied from 32.5 to 33.2 psu. The water along transect S1 was warm and fresh to the north, cold and salty in the middle, and warm and fresh farther to the south. The water was warm and salty to the west, and cold and fresh to the east. The temperature–salinity (T–S) sections (Figures 4 and 5) and T–S diagrams (Figure 6) indicate that there were at least five distinct water masses along transect S1 and three distinct water masses along transect S2. The different water masses might have been formed by different dynamic characteristics.

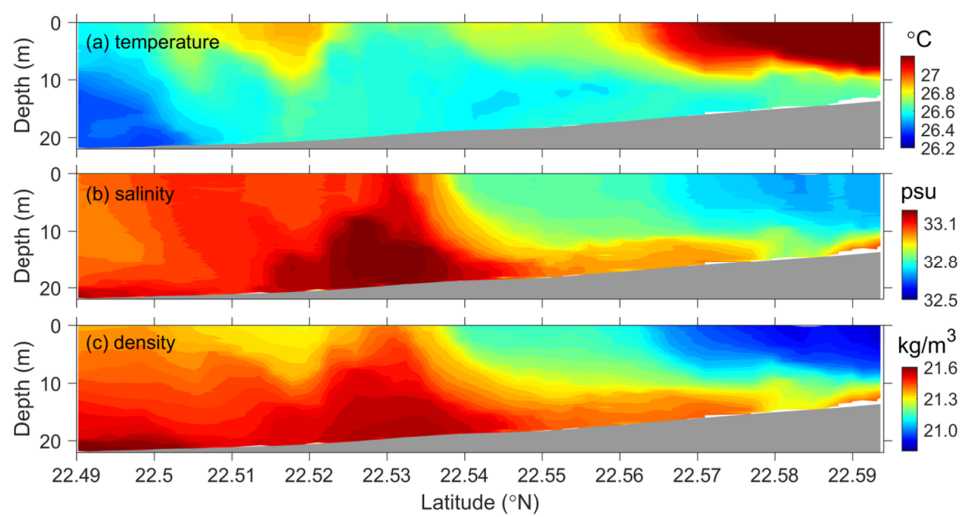


**Figure 4.** (a) Temperature, (b) salinity, and (c) density along transect S1 as measured by the YODA profiler.

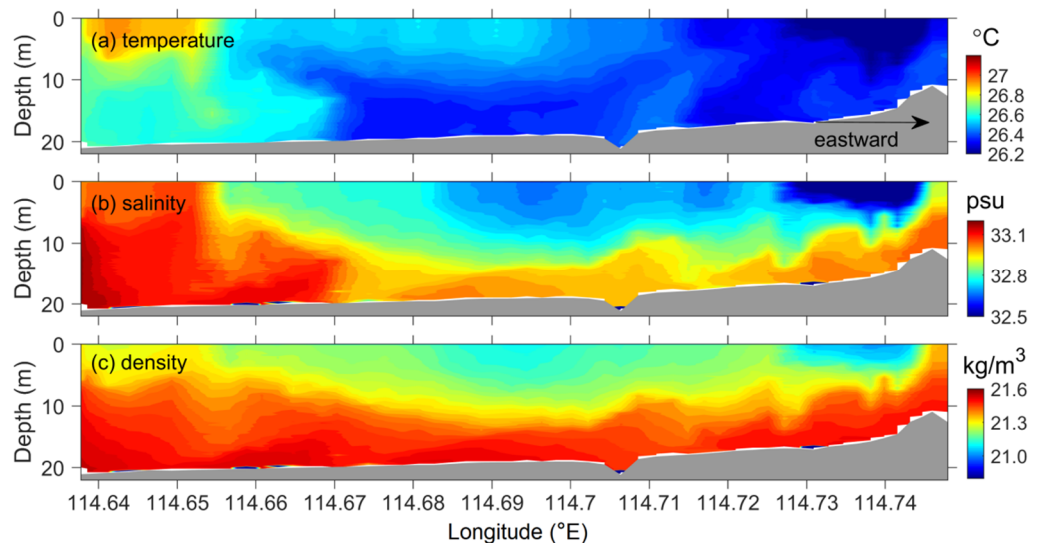


**Figure 5.** (a) Temperature, (b) salinity, and (c) density along transect S2 as measured by the YODA profiler.

The different water masses along transect S1 could be separated into the following five distinct areas. Area 1 had a latitude greater than  $22.56^{\circ}$  N, with warmer and fresher water found at the surface. Water in this area was affected by thermal discharges from the nuclear power station. Area 2 was found between the latitudes  $22.525^{\circ}$  N and  $22.535^{\circ}$  N, with saltier water present throughout the whole depth of the water column and no obvious changes in temperature with depth. Area 3 was found between the latitudes  $22.505^{\circ}$  N and  $22.525^{\circ}$  N, with warmer water present near the surface and no obvious changes in salinity with depth. Area 4 had a latitude lower than  $22.505^{\circ}$  N, with cooler water present throughout the whole depth of the water column. Area 5 was found between the latitudes  $22.535^{\circ}$  N and  $22.56^{\circ}$  N and represented a transition region.

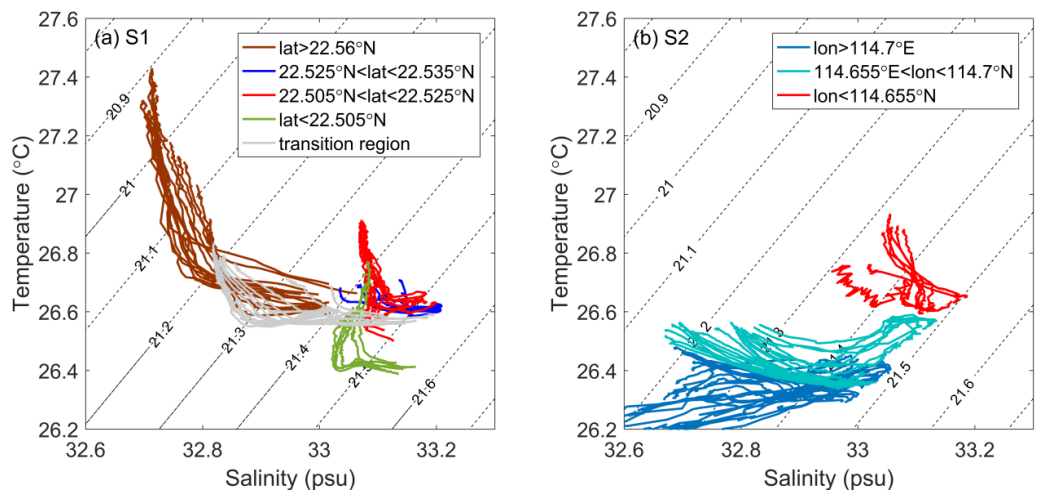


**Figure 6.** Temperature–salinity (T–S) diagrams for transects (a) S1 and (b) S2. Dashed lines indicate potential densities.

The different water masses along transect S2 could be separated into the following three distinct areas. Area 1 had a longitude greater than  $114.7^{\circ}$  E, with cold and fresher water in the upper layer. Area 2 was found between the longitudes  $114.655^{\circ}$  E and  $114.7^{\circ}$  E, with saltier water present near the bottom and no obvious changes in temperature with depth. Area 3 had a longitude less than  $114.655^{\circ}$  E, with warmer and fresher water present near the surface. Generally, water on a shelf is cooler and fresher than in the adjoining ocean, leading to the formation of a shelf break front [26]. Therefore, it was reasonable to assume that the cold water at longitudes greater than  $114.7^{\circ}$  E originated from the bay. The area between  $114.655^{\circ}$  E and  $114.7^{\circ}$  E was considered a transition region.

### 3.1.2. Influence of the Nuclear Power Station

Although the observation area was small, the water characteristics of DYP exhibited obvious spatial variability over a distance of approximately 12.5 km.

A significant feature of water temperature was that it was clearly affected by the thermal discharge from the nuclear power station in the north, and the temperature was significantly higher in the north than in other places (Figure 4a). The surface water temperature was as high as  $27.4^{\circ}\text{C}$  in the northernmost observation position, which was approximately 2 km from the nuclear power station. This was  $1^{\circ}\text{C}$  higher than the water temperature in the south. The warm water from the thermal discharge was mainly concentrated in the upper 10 m and extended approximately 5 km to the south of the release orifice, which corresponded to  $22.56^{\circ}\text{N}$  (Figure 4a). This range at which water discharge from the nuclear power station influenced water temperature was consistent with the satellite remote-sensing study of [10]. It has been reported that during the winter months, the thermal plume formed by water discharge from the nuclear power station is localized to an area within a few kilometers of the power plant. During the summer months, there is a larger thermal plume that extends 8–10 km south along the coast [10]. The strong seasonal difference in the thermal plume is related to vertical mixing in the water column in winter and stratification in summer. In addition to the warm water being discharged from the nuclear power station, a cloud of warm water with a radius of 2 km at the surface between  $22.5^{\circ}\text{N}$  and  $22.52^{\circ}\text{N}$  was also observed. This area of water was  $0.3^{\circ}\text{C}$  warmer than the surrounding water. The temperature difference between the surface and bottom was less than  $1^{\circ}\text{C}$ , indicating weak stratification of the water column during the observation period.

The salinity and chlorophyll-a content were also affected by the power plant. In the area influenced by discharge water, the salinity (Figure 4b) and chlorophyll-a content

(Figure 7c) were lower than in the south. There was no significant difference in DO (Figure 7d).

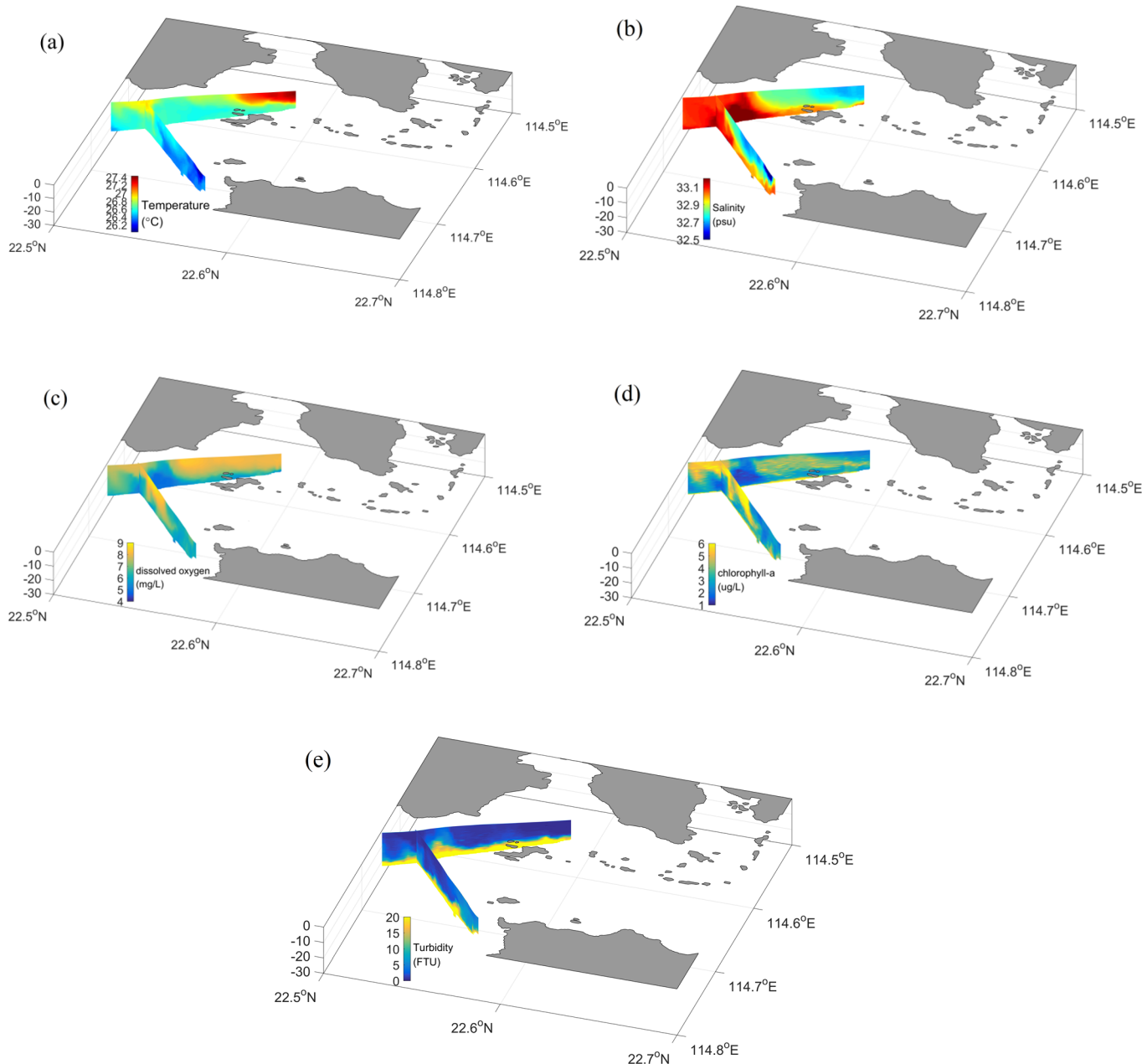


**Figure 7.** Three-dimensional view of (a) temperature, (b) salinity, (c) chlorophyll-a, (d) dissolved oxygen, and (e) turbidity distributions.

### 3.1.3. The Front

Water in DYB is cooler and fresher than in the adjoining SCS, resulting in a strong salinity front that is the most notable hydrographic feature in this region (Figure 4). There was a lateral density gradient identified along both transects S1 and S2. For transect S1, YODA measurements revealed lateral salinity variations as large as 0.7 psu across 1 km between 22.53° N and 22.54° N. Transect S2 also had a similar variation in salinity between 114.65° E and 114.66° E.

The width of the front was approximately 1 km, and the water depth,  $h$ , was 20 m. The Rossby deformation radius  $R = \sqrt{g' h} / f$  was approximately 6 km. The width of the front

was much less than the Rossby deformation radius, indicating that it was not maintained by geostrophic balance. Here,  $g'$  is the reduced gravity, which is given by  $g' = g(r_2 - r_1)/r$ , where  $r_1$  and  $r_2$  are the densities of the upper and lower layers, respectively,  $r$  is the mean density,  $g = 9.81 \text{ m/s}^2$ , and  $f$  is the Coriolis parameter.

In the front area along transect S1, chlorophyll-a increased from 3 to 8 g/L, and the turbidity decreased from 4 to 1 FTU. We assumed that the strong front in S1 was formed at the intersection of different water masses and was strengthened by an upwelling system, in which cooler and saltier water at the bottom was dragged to the upper layer (Section 3.1.4). The presence of the front also prevented water from the adjoining SCS from entering the inner area of DYB.

### 3.1.4. The Upwelling

A cold salty water mass dominated the area between  $22.52^\circ \text{ N}$  and  $22.54^\circ \text{ N}$ . The turbidity was relatively high from the bottom to the sea surface, whereas the DO and chlorophyll-a concentrations were relatively low. The distributions of the parameters indicated a pumping process. The width of the upwelling was approximately 2 km. The most direct evidence of upwelling was the turbidity signal. Figure 7e shows that the turbidity was much higher at depth than in the upper layer. It was induced by friction between water layers, making the water in the bottom boundary layer turbid. In the area between  $22.52^\circ \text{ N}$  and  $22.54^\circ \text{ N}$ , the whole water column was more turbid than the surrounding water. This could only be explained by the turbidity of the entire water body being derived from the turbid water body at the bottom.

The occurrence of an upwelling is closely related to wind conditions. In the Northern Hemisphere, when the wind blows parallel to the coast for a long time, under the action of a geostrophic deflection force, the wind drift formed by the wind causes the surface water to leave the coast. This in turn causes the shallower water near the shore to rise and form an upwelling. In the North SCS, the most notable upwellings are the Eastern Guangdong upwelling and the Eastern Hainan upwelling, which occur in summer months [27–29]. In some case, the wind in particular direction acting on the vorticity field can generate vertical motions. For example, Chang et al. [30] reported that the seaward increasement of cyclonic vorticity near the Kuroshio's western edge favors a stronger Ekman transport away from the jet, producing upwelling at the shelfbreak under a northeasterly wind. The passage of high-energy atmospheric systems also may stir up the upwelling [31]. In this study, however, the upwelling mechanism described above cannot explain the upwelling observed here in October. The upwelling areas caused by large-scale wind fields are more extensive than the upwelling area observed in this study, which had a width of approximately 2 km. The sea surface wind field far from the high-energy atmospheric system during the observation period is also not a cause of the vertical motions of water.

When the surface water is blocked by the coast or an island, sea water will gather and diverge in the horizontal direction, and an upwelling may occur in the vertical direction. In the study region, the terrain is flat in the area where the upwelling was observed (Figure 1), which indicates that the upwelling was induced by other dynamic mechanisms.

We assumed that the upwelling was formed by the interaction between tidal currents and the topography. Upwelling can bring nutrients from the bottom layer to the surface layer, make plankton grow in large quantities, and provide food for fish. Therefore, upwelling areas are often important fishing grounds, such as the Peru fishing grounds, which benefit from the cold Peru Current (upwelling compensation current). In our study area, the upwelling may also have an important impact on the local environment. As shown in Figures 7 and 8, the upwelling changed the distribution of chlorophyll-a and DO in the local area and carried turbid material from the bottom up to the surface.

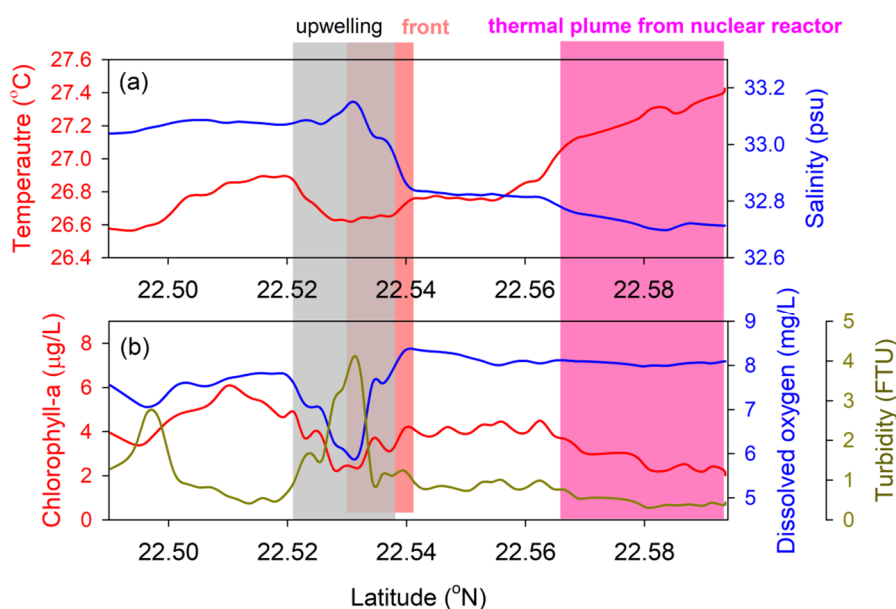


**Figure 8.** (a) Temperature, salinity, (b) chlorophyll-a, dissolved oxygen, and turbidity at a depth of 3 m along transect S1. The filled backgrounds indicate the upwelling (gray), front (orange), and warm discharge water from the nuclear reactor (pink).

### 3.2. High-Resolution Observations by the VMP-250 Profiler

In the section, feature of coastal phenomenon of front and its accompanied turbulence are revealed by high temporal resolution observations by YODA.

#### 3.2.1. Water Properties

We used the VMP-250 profiler to observe turbulence for 22 h at a fixed location and obtained 74 profiles. The time intervals varied between 10 and 30 min (Figure 9c). A nose-mounted conductivity–temperature sensor was installed on the VMP-250 profiler, enabling the analysis of temperature and salinity characteristics observed at continuous monitoring stations.

The measurements indicated that both the temperature and salinity changed rapidly with time. Using density data, we calculated the depth of the surface mixed layer and the thickness of the bottom mixed layer (Figure 9c). The depth of the mixed layer was defined as the point at which the density varied by less than  $0.05 \text{ kg/m}^3$ . The depth of the upper mixed layer was 8 m, whereas the thickness of the bottom mixed layer extended to 8 m (the water depth at the observation station was ca. 20 m). Sometimes, a bottom mixed layer could not be discerned. Activities in the upper water extended to the sea bottom at times (e.g., at 20:00 on 21 October 2015). The bottom mixed layer was mainly affected by tides, with the mixed layer depth increasing at high tide (Figure 9c,f). The largest buoyancy fluxes were in the stratified region just above the bottom mixed layer (Figure 9d).

The T-S sections and T-S diagrams (Figure 10) indicate that the water masses at various stations comprised distinct water masses. For example, between 21:00 on 21 October 2015 and 3:00 on 22 October 2015, the water temperature was low and salinity was high, especially in the bottom mixed layer. This was a period of high tide, indicating that SCS water was dominant during this period. From 6:00 to 8:00 on 22 October 2015, the upper layer of water exhibited a low temperature and low salinity. This was the ebb tide period, indicating that DYB water was the dominant water mass. Compared with the Figure 6, the characteristics of the seawater was confirmed. The observation station was located at the confluence of the SCS and DYB, which changed constantly under the action of tides. With the interactions at the confluence, an abundance of thermohaline structures was formed.

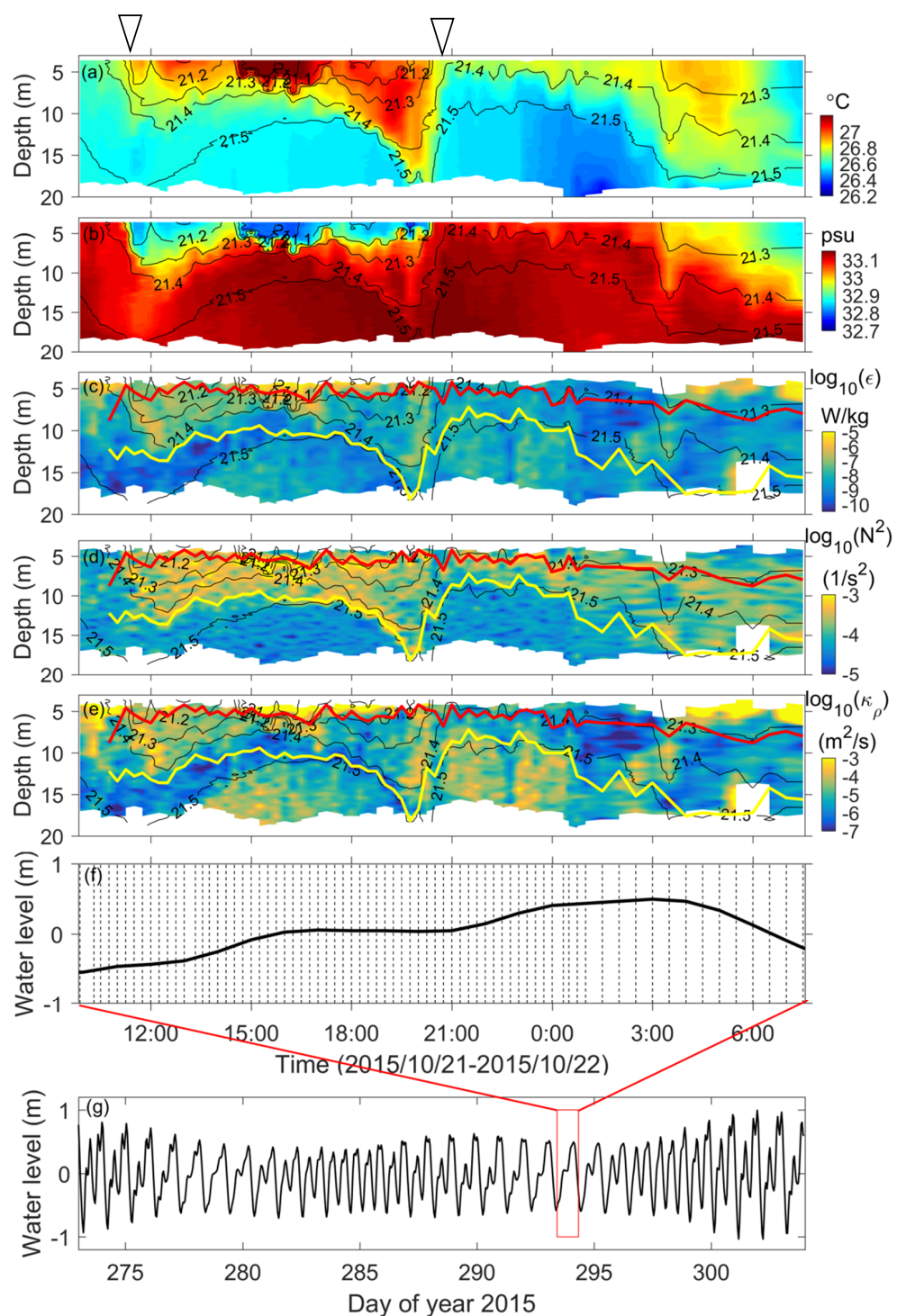


**Figure 9.** Time courses of (a) temperature, (b) salinity, (c) dissipation rate, (d) buoyancy frequency, (e) diffusivity, (f) water level during the observation periods, and (g) water level of October 2015. Isopycnal contours (solid lines) in (a–e) represent density. The front is marked with an inverted triangle in (a). In (c–e), the red line indicates the surface mixed layer, whereas the yellow line indicates the bottom mixed layer. Vertical dotted lines in (f) indicate the time points of VMP-250 observations. The water-level data in (f,g) were derived at the tidal elevation station T1.

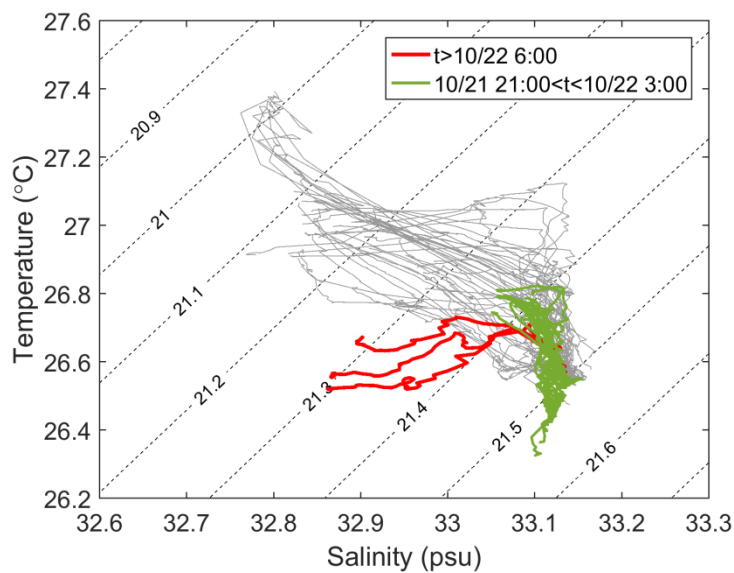


**Figure 10.** T-S diagram of VMP-250 measurements. Dashed lines indicate potential densities.

### 3.2.2. The Front

In addition to YODA measurements, lateral density gradients were also identified in the study area from the fixed station observations (Figure 9). These gradients were controlled by variations in both salinity and temperature. Stratification persisted throughout the upper water column, with considerable variability along isopycnal. VMP-250 measurements indicated lateral temperature variations as large as  $0.4\text{ }^{\circ}\text{C}$  and lateral salinity variations as large as  $0.3\text{ psu}$  over 30-min periods at 11:30 and 20:30 on 21 October 2015. It is noted that the conventional definition of density front ( $d\rho/dx$ ) is related to the variation of horizontal distance of density. Here, we assume that the density front does not change in a certain period of time when it moves in the flow direction,  $d\rho/dt = U d\rho/dx$ . Thus, the larger the variation in  $d\rho/dt$ , the stronger the density front. There were two strong fronts at these two moments, with density variations of approximately  $0.2\text{ kg/m}^3$  over a 30-min period. At 20:30 on 21 October 2015, the front extended to the bottom. The width of the front was approximately 1 km (Section 3.1.3), and it took approximately 30 min for the front to cross the observation position. Therefore, we inferred that the speed of the front was approximately  $0.5\text{ m/s}$ , which is similar to the tidal current velocity [18].

### 3.2.3. Turbulence

Examples of dissipation spectra at specified depth segments from the VMP-250 measurement at 12:15 on 21 October 2015 are shown in Figure 11. There were two shear probes installed at the head of profiler, and data from both probes are shown. The spectra were approximately consistent with the Nasmyth universal spectrum, indicating the credibility of the measurement. The triangles indicate the upper limit of integration. The raw microscale velocity shear was weak between 4 and 8 m; therefore, the estimated dissipation rate was small ( $\varepsilon \sim 10^{-7}\text{ W/kg}$ ). The microscale velocity shear strengthened between 8 and 12 m, as did the dissipation ( $\varepsilon \sim 10^{-6}\text{ W/kg}$ ).

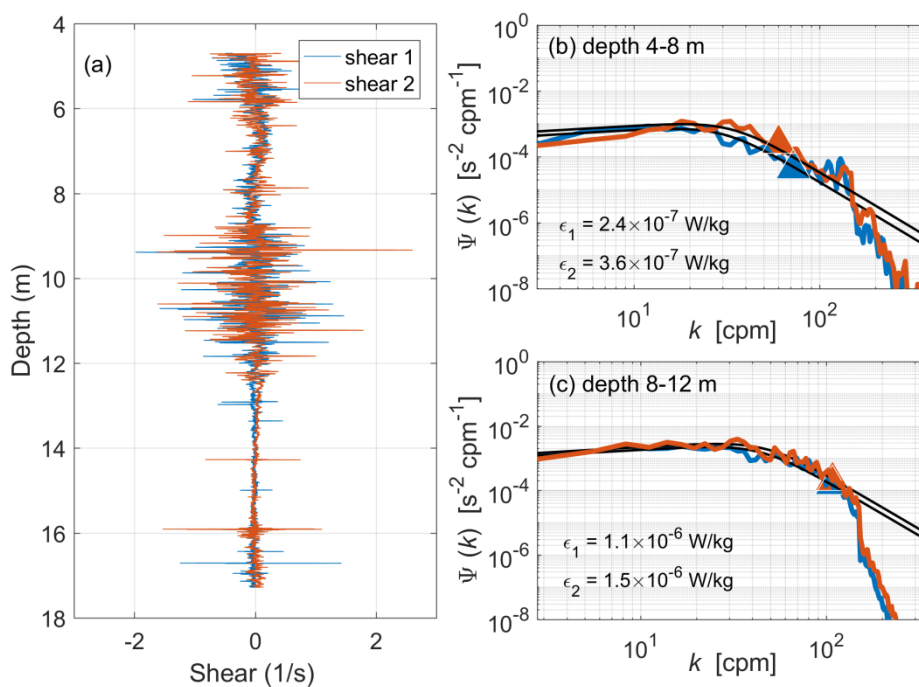


**Figure 11.** (a) Examples of raw microscale velocity shear in specified depth segments during data recording at 12:15 on 21 October 2015 and (b,c) the corresponding dissipation spectra. The smooth curves overlapping the dissipation spectra represent the Nasmyth universal spectrum, and triangles indicate the upper limit of integration.

It has been reported that dissipation and mixing on the shelf are mainly controlled by near-bottom friction and shear from low-frequency internal waves and solibores [26]. However, according to our observations, the front that formed at the intersection of the SCS and DYB also plays an important role in local energy dissipation. Figure 9c shows the dissipation rates and associated diapycnal diffusivities for each profile. The dissipation rates of the thermocline and bottom boundary layer were of the same order of magnitude. The thickness of the bottom mixing layer has the characteristics of periodic variation, and its increase is consistent with the period of high tide. The dissipation rate at the bottom also increase during the high tide periods (Figure 9e). Taken together with Figure 9c,e,f, it was concluded that the turbulence in the bottom mixed layer was driven by tidal currents. In the upper mixing layer, ocean mixing is mainly controlled by buoyancy flux and wind momentum flux [32]. In this study, we focused on the dissipation in the thermocline.

The dissipation rate of the thermocline was mainly between  $1 \times 10^{-9}$  and  $1 \times 10^{-6}$  W/kg, with an average value of  $8 \times 10^{-8}$  W/kg. The maximum value was mainly recorded at 11:30, 16:00, and 20:30 on 21 October 2015, as well as 3:00 on 22 October 2015, at which point the density profile changed substantially. Peak dissipation at 5:00 on 22 October 2015 was induced in a patch near the bottom. Average diffusivity profiles were calculated from the average dissipation rate and stratification. Because diffusivity was not well defined in the well-mixed boundary layers, average diffusivity profiles are only shown for data excluding the boundary layer (Figure 12a). The average diffusivity associated with mid-column, stratified turbulence was  $5.8 \times 10^{-5}$  m<sup>2</sup>/s for the whole profile, which is one order of magnitude greater than the level in an open-ocean thermocline [33,34].

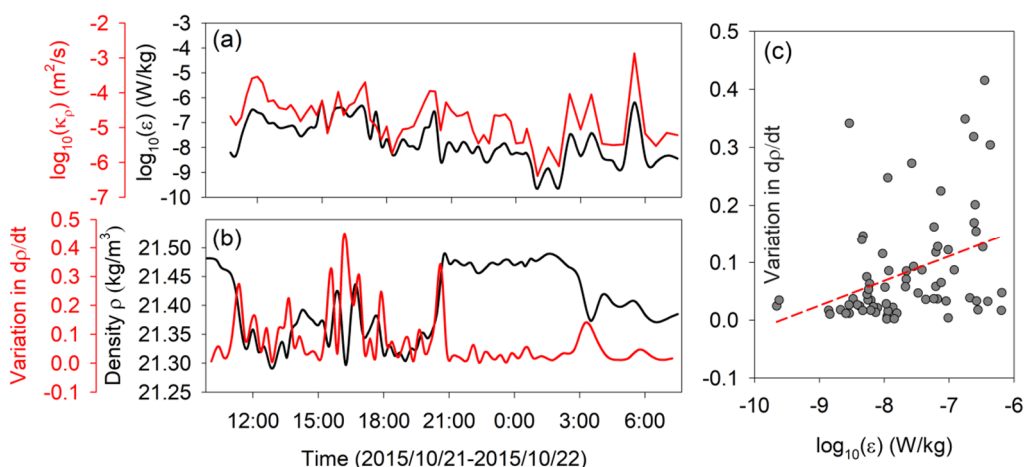


**Figure 12.** Time courses of the (a) average dissipation rate and diffusivity, and (b) average density and variation in  $d\rho/dt$ . (c) Relationship between the dissipation rate and variation in  $d\rho/dt$ .

To analyze the relationship between front and turbulent mixing in the thermocline, the density of water was averaged, excluding the boundary layer. Changes in average density with time ( $d\rho/dt$ ) were calculated. Active fronts existed on 21 November but there were fewer fronts on 22 November (Figure 12b). The fronts detected between 15:00 and 18:00 on 21 October 2015 were affected by the variation in density near the surface mixed layer. It can be seen from Figure 10 that the dissipation rate and variation in  $d\rho/dt$  were positively correlated, i.e., a larger  $d\rho/dt$  tended to produce a larger dissipation rate. This indicates that a density front in the study area is important for locating the sources of energy dissipation.

The turbulent mixing process in the ocean determines the redistribution of seawater characteristics. This plays a key role in the redistribution of nutrients, DO, and other ecological elements and substances in the ocean, which then affects marine productivity [35–38]. In this study, we did not make observations of ecological elements when VMP-250 measurements were recorded. However, it was apparent that the front regulated the distribution of ecological elements (Figure 7), while turbulent mixing also played an important role.

#### 4. Discussion

##### Comparison with Observations in July 2019

Daya Bay is located in the tropical monsoon region. In this area, the northeast monsoon is strong in winter, whereas the weaker southwest monsoon is dominant in summer [39]. During winter, the water in DYB is vertically mixed under the influence of the northeast monsoon [40]. Water stratification in DYB varies seasonally. The development of physical phenomena in the ocean is closely related to stratification, and seasonal variation in the formation of a front and its effect on energy dissipation in the observation area was obvious.

To confirm the seasonal variation in the front in DYB, we analyzed observations of the area ( $114.68^\circ \text{E}, 22.58^\circ \text{N}$ ) from July 2019 (Figure 1). At the observation site, 138 profiles were obtained by YODA within 48 h, with a time interval of 20 min. The temperature difference between the surface and bottom was more than  $6^\circ\text{C}$ , and the salinity difference was more than 2 psu (Figure 13), which were much larger than the values measured in October (Figure 10). The fresh water input during the summer rainy season diminished the surface salinity, and water with a lower temperature and high salinity intruded into the bay along the bottom from the SCS. Unlike the observations made in October, there was a stable bottom mixed layer in July that was more than 10 m thick (Figure 13d). Above the bottom mixing layer was a thermocline reflecting strong stratification. In the July 2019 observations, there was no obvious density front, but a high-frequency internal wave at the thermocline was observed. As shown in Figure 13c, the density (in the region of  $1022.5 \text{ kg/m}^3$ ) oscillated within a thickness of 4 m in the thermocline. According to

observations from October 2015, vertical fluctuation of the isotherm exceeded 10 m, and the density changed substantially at different times and at certain depths.

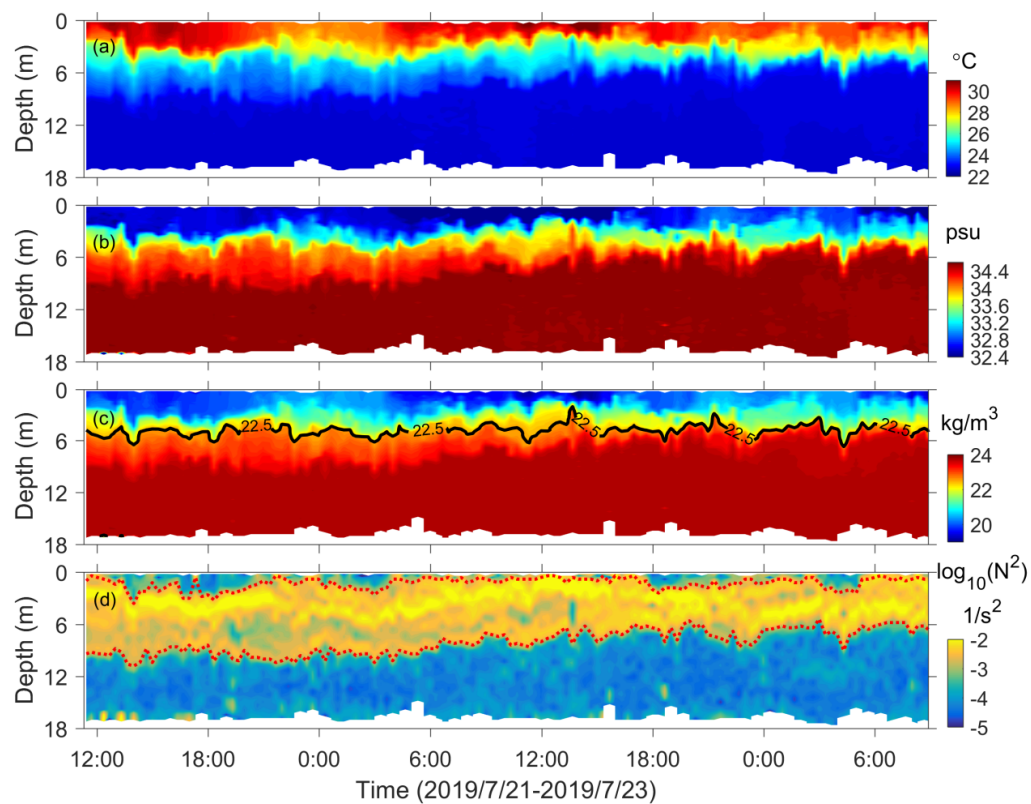


**Figure 13.** Time courses of (a) temperature, (b) salinity, (c) density, and (d) buoyancy frequency as measured by YODA in July 2019. The black line in (c) indicates a density of  $1022.5 \text{ kg/m}^3$ . Red dotted lines in (d) indicate the surface and bottom mixed layers.

In autumn, the upwelling along the coast of Guangdong disappeared due to the transition of the monsoon. Low-temperature and high-salinity water could not intrude into the bay along the bottom from the SCS, leading to the temperature and salinity of the bottom water being warmer and lower, respectively, than in summer (Figures 9 and 13). The larger temperature and salinity differences between the surface and bottom in summer led to stronger stratification in July 2019 compared to October 2015. As shown in Figure 14, the buoyancy frequency in summer in the thermocline was more than one order of magnitude higher. The strong stratification prevented the upper dynamic waves from crossing the thermocline, and the front was absent in summer. Thus, it was concluded that weak stratification in autumn is important for the formation of a front. In the final analysis, the transition of the monsoon was the primary factor causing changes in stratification.

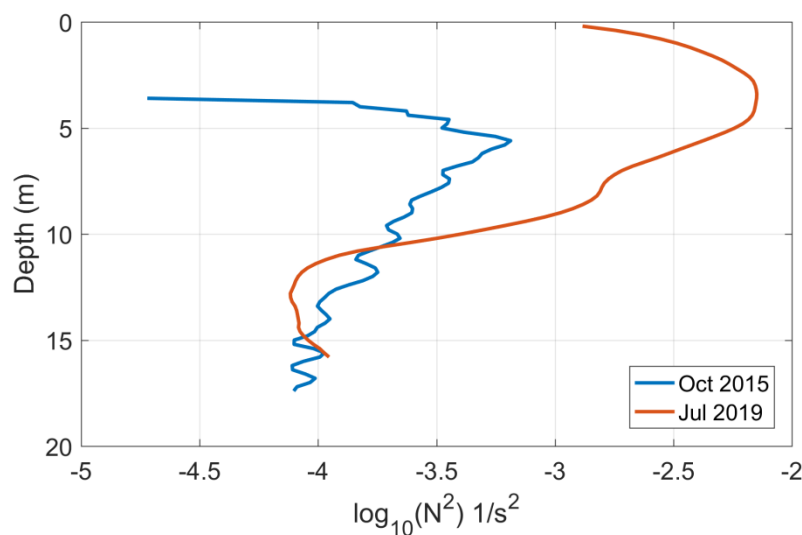


**Figure 14.** Averaged profiles of buoyancy frequency measured in October 2015 (summer) and July 2019 (autumn).

## 5. Conclusions

We used a tow-yo CTD instrument, the YODA profiler, to record high-resolution physical and biological data in DYB from a small vessel in October 2015. Observations in the DYB revealed complex coastal phenomena, which included warm-water discharge from a nuclear plant, as well as an upwelling, and strong density front. Those coastal phenomena changed the distribution of ecological elements. The upwelling resulted in saltier and more turbid water near the bottom, with low chlorophyll-a and DO contents, being transported upward to the surface layer and changing the local water environment. The front had a width of 1 km and formed at the intersection of the SCS and DYB. It was strengthened by the upwelling system.

Turbulence over a 22-h period at the mouth of DYB was also observed by using a microstructure turbulence profiler. The water column was divided into a surface mixed layer, thermocline, and bottom mixed layer. The turbulence was focused within the thermocline. The dissipation rate and diapycnal diffusivity in the thermocline displayed clear variability. The average (in time and space) dissipation rate and diapycnal diffusivity in the thermocline were  $8 \times 10^{-8} \text{ W/kg}$  and  $5.8 \times 10^{-5} \text{ m}^2/\text{s}$ , respectively, which were one order of magnitude larger than the respective levels in an open-ocean thermocline. Active density fronts were observed in the thermocline and were associated with strong turbulent mixing. The active front was induced by weak stratification during the observation period. The results indicate that, rather than internal waves, it was the front that had formed at the intersection of different water bodies that played the primary role in energy dissipation at the mouth of DYB.

**Author Contributions:** Conceptualization, Y.Q.; methodology, Y.Q.; validation, X.W.; formal analysis, C.Q.; investigation, L.Y., X.W., and X.S. and X.C.; data curation, Y.Q.; writing—original draft preparation, H.M.; writing—review and editing, H.M.; supervision, S.L. and Z.L.; project administration, H.M.; funding acquisition, S.L. All authors have read and agreed to the published version of the manuscript.

**Funding:** This study is supported by the National Key R&D Plan of China under contract Nos 2017YFC0305904, 2017YFC0305804 and 2016YFC1401404; the National Natural Science Foundation of China under contract Nos 42006020, 41630970, and 41806037; the Guangdong Science and Technology Project under contract Nos 2019A1515111044 and 2018A0303130047; the Dedicated Fund for Promoting High-quality Economic Development in Guangdong Province (Marine Economic Development Project) under contract No. GDOE[2019]A03; the CAS Key Technology Talent Program (202012292205).

**Institutional Review Board Statement:** Not applicable.

**Informed Consent Statement:** Not applicable.

**Data Availability Statement:** Not applicable.

**Conflicts of Interest:** The authors declare no conflict of interest.

## References

1. Liu, W.T.; Xie, X. Spacebased observations of the seasonal changes of south Asian monsoons and oceanic responses. *Geophys. Res. Lett.* **1999**, *26*, 1473–1476. [[CrossRef](#)]
2. Xie, S.-P.; Xie, Q.; Wang, D.; Liu, W.T. Summer upwelling in the South China Sea and its role in regional climate variations. *J. Geophys. Res. Space Phys.* **2003**, *108*, 3261. [[CrossRef](#)]
3. Shaw, P.-T.; Chao, S.-Y. Surface circulation in the South China Sea. *Deep. Sea Res. Part I Oceanogr. Res. Pap.* **1994**, *41*, 1663–1683. [[CrossRef](#)]
4. Fang, W.; Huang, Q.; Shi, P.; Xie, Q. Seasonal structures of upper layer circulation in the southern South China Sea from in situ observations. *J. Geophys. Res. Space Phys.* **2002**, *107*, 23-1. [[CrossRef](#)]
5. Qu, T. Upper-layer circulation in the South China Sea. *J. Phys. Oceanogr.* **2000**, *30*, 1450–1460. [[CrossRef](#)]
6. Qu, T.; Du, Y.; Gan, J.; Wang, D. Mean seasonal cycle of isothermal depth in the South China Sea. *J. Geophys. Res. Space Phys.* **2007**, *112*, 02020. [[CrossRef](#)]
7. Zhang, Z.; Zhao, W.; Qiu, B.; Tian, J. Anticyclonic Eddy Sheddings from Kuroshio Loop and the Accompanying Cyclonic Eddy in the Northeastern South China Sea. *J. Phys. Oceanogr.* **2017**, *47*, 1243–1259. [[CrossRef](#)]
8. Hu, J.; Kawamura, H.; Hong, H.; Qi, Y. A review on the currents in the South China Sea: Seasonal circulation, South China Sea warm current and Kuroshio intrusion. *J. Oceanogr.* **2000**, *56*, 607–624. [[CrossRef](#)]
9. Xiu, P.; Chai, F.; Shi, L.; Xue, H.; Chao, Y. A census of eddy activities in the South China Sea during 1993–2007. *J. Geophys. Res. Ocean.* **2010**, *115*. [[CrossRef](#)]
10. Tang, D.; Kester, D.R.; Wang, Z.; Lian, J.; Kawamura, H. AVHRR satellite remote sensing and shipboard measurements of the thermal plume from the Daya Bay, nuclear power station, China. *Remote. Sens. Environ.* **2003**, *84*, 506–515. [[CrossRef](#)]
11. Masunaga, E.; Yamazaki, H. A new tow-yo instrument to observe high-resolution coastal phenomena. *J. Mar. Syst.* **2014**, *129*, 425–436. [[CrossRef](#)]
12. Ozer, T.; Gertman, I.; Kress, N.; Silverman, J.; Herut, B. Interannual thermohaline (1979–2014) and nutrient (2002–2014) dynamics in the Levantine surface and intermediate water masses, SE Mediterranean Sea. *Global Planet. Chang.* **2017**, *151*, 60–67. [[CrossRef](#)]
13. Castelao, R.M.; Mavor, T.P.; Barth, J.A.; Breaker, L.C. Sea surface temperature fronts in the California Current System from geostationary satellite observations. *J. Geophys. Res. Oceans* **2006**, *111*. [[CrossRef](#)]
14. Arnone, R.A.; La Violette, P.E. Satellite definition of the bio-optical and thermal variation of coastal eddies associated with the African Current. *J. Geophys. Res. Space Phys.* **1986**, *91*, 2351. [[CrossRef](#)]
15. Turrin, J.; Forster, R.R.; Larsen, C.; Sauber, J. The propagation of a surge front on Bering Glacier, Alaska, 2001–2011. *Ann. Glaciol.* **2013**, *54*, 221–228. [[CrossRef](#)]
16. Moum, J.N.; Farmer, D.M.; Smyth, W.D.; Armi, L.; Vagle, S. Structure and generation of turbulence at interfaces strained by internal solitary waves propagating shoreward over the continental shelf. *J. Phys. Oceanogr.* **2003**, *33*, 2093–2112. [[CrossRef](#)]
17. Van Haren, H. Using high sampling-rate ADCP for observing vigorous processes above sloping [deep] ocean bottoms. *J. Mar. Syst.* **2009**, *77*, 418–427. [[CrossRef](#)]
18. Song, D.; Yan, Y.; Wu, W.; Diao, X.; Ding, Y.; Bao, X. Tidal distortion caused by the resonance of sexta-diurnal tides in a micromesotidal embayment. *J. Geophys. Res. Oceans* **2016**, *121*, 7599–7618. [[CrossRef](#)]
19. Sun, C.-C.; Wang, Y.-S.; Wu, M.-L.; Dong, J.-D.; Wang, Y.-T.; Sun, F.-L.; Zhang, Y.-Y. Seasonal Variation of Water Quality and Phytoplankton Response Patterns in Daya Bay, China. *Int. J. Environ. Res. Public Health* **2011**, *8*, 951. [[CrossRef](#)] [[PubMed](#)]
20. Liao, X.L.; Chen, P.M.; Ma, S.W.; Chen, H.G. Community structure and environmental adaptation of phytoplankton in Yangmeikeng artificial reef area in Daya Bay, South China Sea. *Adv. Mater. Res.* **2013**, *807–809*, 52–60. [[CrossRef](#)]
21. Wu, M.L.; Wang, Y.T.; Wang, Y.S.; Sun, F.L. Influence of environmental changes on picophytoplankton and bacteria in Daya Bay, South China Sea. *Cienc. Mar.* **2013**, *40*, 197–210. [[CrossRef](#)]
22. Yang, X.; Tan, Y.; Li, K.; Zhang, H.; Liu, J.; Xiang, C. Long-term changes in summer phytoplankton communities and their influencing factors in Daya Bay, China (1991–2017). *Mar. Pollut. Bull.* **2020**, *161*, 111694. [[CrossRef](#)] [[PubMed](#)]
23. Osborn, T.R. Estimates of the local-rate of vertical diffusion from dissipation measurements. *J. Phys. Oceanogr.* **1980**, *10*, 83–89. [[CrossRef](#)]
24. Shang, X.; Qi, Y.; Chen, G.; Liang, C.; Lueck, R.G.; Prairie, B.; Li, H. An Expendable Microstructure Profiler for Deep Ocean Measurements. *J. Atmospheric Ocean. Technol.* **2017**, *34*, 153–165. [[CrossRef](#)]
25. Lueck, R.G. Calculating the Rate of Dissipation of Turbulent Kinetic Energy. Rockland Scientific International Tech. Note TN-028. 2015. 18p. Available online: <https://rocklandsientific.com/support/knowledge-base/technical-notes/> (accessed on 13 May 2021).
26. MacKinnon, J.A.; Gregg, M.C. Mixing on the late-summer NewEngland shelf—Solibores, shear, and stratification. *J. Phys. Oceanogr.* **2003**, *33*, 1476–1492. [[CrossRef](#)]

27. Gu, Y.; Pan, J.; Lin, H. Remote sensing observation and numerical modeling of an upwelling jet in Guangdong coastal water. *J. Geophys. Res. Space Phys.* **2012**, *117*, 08019. [[CrossRef](#)]
28. Hu, J.; Wang, X.H. Progress on upwelling studies in the China seas. *Rev. Geophys.* **2016**, *54*, 653–673. [[CrossRef](#)]
29. Jing, Z.-Y.; Qi, Y.-Q.; Hua, Z.-L.; Zhang, H. Numerical study on the summer upwelling system in the northern continental shelf of the South China Sea. *Cont. Shelf Res.* **2009**, *29*, 467–478. [[CrossRef](#)]
30. Chang, Y.-L.; Oey, L.-Y.; Wu, C.-R.; Lu, H.-F. Why Are There Upwellings on the Northern Shelf of Taiwan under Northeasterly Winds? *J. Phys. Oceanogr.* **2010**, *40*, 1405–1417. [[CrossRef](#)]
31. Jolliff, J.K.; Jarosz, E.; Ladner, S.; Smith, T.; Anderson, S.; Dykes, J. The Optical Signature of a Bottom Boundary Layer Ventilation Event in the Northern Gulf of Mexico’s Hypoxic Zone. *Geophys. Res. Lett.* **2018**, *45*, 8390–8398. [[CrossRef](#)]
32. Liang, C.-R.; Chen, G.-Y.; Shang, X.-D. Observations of the turbulent kinetic energy dissipation rate in the upper central South China Sea. *Ocean Dyn.* **2017**, *67*, 597–609. [[CrossRef](#)]
33. Polzin, K.L.; Toole, J.M.; Schmitt, R.W. Finescale parameterizations of turbulent dissipation. *J. Phys. Oceanogr.* **1995**, *25*, 306–328. [[CrossRef](#)]
34. Liang, C.R.; Shang, X.D.; Qi, Y.F.; Chen, G.Y.; Yu, L.H. Assessment of fine-scale parameterizations at low latitudes of the North Pacific. *Sci. Rep.* **2018**, *8*, 1–10. [[CrossRef](#)] [[PubMed](#)]
35. Munk, W.H.; Munk, W.; Wunsch, C. Abyssal recipes II: Energetics of tidal and wind mixing. *Deep. Sea Res. Part I Oceanogr. Res. Pap.* **1998**, *45*, 1977–2010. [[CrossRef](#)]
36. Wunsch, C.; Ferrari, R. Vertical Mixing, Energy, And The General Circulation Of The Oceans. *Annu. Rev. Fluid Mech.* **2004**, *36*, 281–314. [[CrossRef](#)]
37. Ganachaud, A.; Wunsch, C. Improved estimates of global ocean circulations, heattransport and mixing from hydrographic data. *Nature* **2000**, *408*, 453–456. [[CrossRef](#)]
38. Garrett, C. Mixing with latitude. *Nat. Cell Biol.* **2003**, *422*, 477. [[CrossRef](#)]
39. Tang, D.L.; Ni, I.H. Remote sensing of Hong Kong waters: Spatial and temporal changes of sea surface temperature. *Acta Oceanogr. Taiwanica* **1996**, *35*, 173–186.
40. Zhan, B.; Zeng, G.; Li, L. Temperature and salinity of Daya Bay. In *Collections of Papers on Marine Ecology in the Daya Bay (II)*; Third Institute of Oceanography, SOA, Ed.; Ocean Publishing House: Beijing, China, 1990; pp. 67–74. (In Chinese)